ChemElectroChem

Research Article
doi.org/10.1002/celc.202300549

Chemistry Europe
European Chemical Societies Publishing

www.chemelectrochem.org

Effect of Carbon Xerogel Activation on Fe–N–C Catalyst Activity in Fuel Cells

Laura Álvarez-Manuel,[a] Cinthia Alegre,*[a] David Sebastián,*[a] Pedro F. Napal,[a] Cristina Moreno,[a] Esther Bailón-García,[b] Francisco Carrasco-Marín,[b] and María J. Lázaro[a]

Fe–N–C catalysts are an interesting option for polymer electrolyte fuel cells due to their low cost and high activity towards the oxygen reduction reaction (ORR). Since Fe–N–C active sites are preferentially formed in the micropores of the carbon matrix, increasing the microporosity is highly appealing. In this work, carbon xerogels (CXG) were activated by physical and chemical methods to favor the formation of micropores, used as carbon matrices for Fe–N–C catalysts, and investigated for the ORR. The catalysts were characterized by solid-state techniques to determine chemical composition and pore structure. Physical activation increased microporosity up to 2-fold leading to catalysts with a larger density of active sites (more than twice iron and nitrogen uptake, pyridinic N and Nx–Fe). This entailed a higher ORR intrinsic activity determined in a 3-electrode cell (80 mV better half-wave potential). At the cathode of a fuel cell, the catalysts based on activated carbon materials showed 26% lower power density ascribed to a more hydrophilic surface, causing a larger extent of flooding of the electrode that counterbalances the higher intrinsic activity. Interestingly, a more stable behavior was observed for the activated catalysts, with up to 2-fold better relative power density retention after 20-hour operation.

Introduction

Fe–N–C catalysts have received extraordinary interest from the scientific community as an alternative to Pt-based catalysts for polymer electrolyte fuel cells (PEFC). These catalysts have reached comparable or even superior activities than Pt-based catalysts for the oxygen reduction reaction (ORR), especially in alkaline electrolytes, but also in the more challenging acidic environment (proton exchange membrane).[1–4]

There is a wide variety of synthesis methods to obtain highly active Fe–N–C catalysts, many of them relying on sacrificial hard-template routes.[5–7] In order to obtain an adequate porous structure that balances porosity in the entire range (micro-, meso- and macro-porosity), several Fe–N–C catalyst synthesis routes have been developed in recent years. For example, many Fe–N–C catalysts are obtained using template-based methods using a variety of carbon and nitrogen precursors.[8–10] This method allows controlling the porosity of the catalyst, varying the size of the silica precursor. However, the utilization of soft or hard templates entails processing and environmental issues, since toxic reagents are needed to remove the templates.[11] Other authors employ metal-organic-frameworks (MOFs) with large porosities and containing iron and nitrogen precursors, to provide access to the Fe–Nx centres. However, MOFs are usually expensive. In this regard, template-free methods are highly appealing, including those using inexpensive carbon precursors for Fe–N–C catalysts with an easily adjustable porosity.

It is widely acknowledged that Fe–N_4 sites are the most active and selective centers towards ORR,[10,12–14] being formed preferentially in the micropores of the carbon matrix,[15].[16] Therefore, tailoring microporosity is a key factor in the design of Fe–N–C catalysts.[17] Novel promising preparation strategies consider low-cost precursors derived from biomass (soybeans, grapefruit peel, or waste reed) leading to active Fe–N–C catalysts.[18,19] In this approach, the porosity is unfortunately not easy to be tuned since it depends on the characteristics of the biomass source.

In this context, the use of synthetic carbon materials, in particular carbon gels, as matrices for Fe–N–C catalysts is an interesting approach, due to their easily tailored 3D porosity, excellent conductivity and their tuneable surface chemistry.[20] Their porous structure can be obtained through template-free methods, avoiding the problems associated to the removal of the template in template-based methods. Another advantage of carbon gels is that their textural properties are controlled by the sol-gel synthesis process, and besides, microporosity can be further tailored by activation procedures.[21] Activation methods are classified into two types: physical (using, for example, steam, CO_2 or O_2 at high temperature) and chemical (using, for example, KOH or $ZnCl_2$).[22] Chemical activation has certain advantages over physical activation: i) lower temperatures and

[a] L. Álvarez-Manuel, Dr. C. Alegre, Dr. D. Sebastián, P. F. Napal, C. Moreno, Prof. M. J. Lázaro
Instituto de Carboquímica, Consejo Superior de Investigaciones Científicas
C/. Miguel Luesma Castán, 4, 50018 Zaragoza, Spain
E-mail: cinthia@icb.csic.es
dsebastian@icb.csic.es

[b] Dr. E. Bailón-García, Prof. F. Carrasco-Marín
Laboratorio de Materiales Polifuncionales Basados en Carbono. Departamento de Química Inorgánica, Facultad de Ciencias – Unidad de Excelencia Química Aplicada a Biomedicina y Medioambiente" Universidad de Granada (UEQ-UGR), 18071 Granada, Spain

Supporting information for this article is available on the WWW under https://doi.org/10.1002/celc.202300549

shorter times are required, ii) activation is carried out in a single step, iii) high yields are obtained. On the contrary, chemical activation has certain disadvantages, such as the need to wash the obtained material after activation and the more corrosive nature of the chemical agents used as activators, that can change the surface chemistry.[23] An appropriate selection of the activation process is essential to tailor the microporosity of the carbon material.[24] Since an excessive increase in microporosity coming from narrow pores, would be inaccessible to protons and oxygen molecules, not leading to better oxygen activity.

According to the low-cost strategy in the synthesis of Fe–N–C catalysts, in this work we propose the use of carbon xerogels (CXG) as low-cost carbon matrix for Fe–N–C catalysts. CXG were doped with nitrogen by means of impregnation with urea, a low-cost and abundant nitrogen precursor, easier to handle than other usually employed, such as NH_3.[25–27] In order to increase the amount of active sites, the microporosity of the carbon materials was modified by activation methods: CO_2, H_2O (vapour) and KOH. The effect of the different activation treatments on the ORR catalytic activity of the Fe–N–C catalysts was assessed in a half-cell in acidic media. Since the results obtained in ideal three-electrode systems are not always transferable to the performance in real applications, the performance and durability of the Fe–N–CXG catalysts were also studied at the cathode of a hydrogen-fed fuel cell (single cell configuration).[28–31]

Experimental

Carbon xerogels synthesis

Carbon xerogels were obtained from the polymerization and pyrolysis of resorcinol (R) and formaldehyde (F) mixtures.[32,33] R/F molar ratio selected was 0.5 with a dilution ratio of 5.7.[34] As in previous works, resorcinol (98%, Sigma-Aldrich) was dissolved in deionized water. Afterwards, formaldehyde (37 wt.% in H_2O, incl. 10%–15% methanol, Sigma-Aldrich) was added to the resorcinol aqueous solution and stirred for 5 minutes. The pH of this solution (3.8) was adjusted to 5.2 adding some drops of a 1 M NaOH (99.99% Alfa-Aesar) aqueous solution. The obtained mixture was transferred into glass vials that were placed in a stove for curing (gelation) for 24 h at 25 °C, 24 h at 50 °C, and 72 h at 85 °C.[35] After this, the so-obtained organic gels were immersed in ethanol for three days, this ethanol was exchanged three times every 24 h. The aim of this treatment is to preserve the original porous structure of the organic material. After grinding the soaked organic gels in a mortar, they were dried in a stove with convective drying at 65 °C and at 110 °C, 5 hours at each temperature. The dried powder obtained was further milled at 150 rpm in a planetary ball mill for 90 minutes. Pyrolysis of the organic dried gels was performed in inert (N_2) atmosphere in a Khantal tubular reactor at 800 °C for 120 minutes.[32]

Carbon xerogels activation

The previously synthesized carbon xerogels were activated by physical and chemical methods.[22,36] Physical methods included activation by CO_2 or water steam (H_2O), whereas the chemical activation was performed with KOH. The percentage of activation, also known as burn-off, was calculated by dividing the mass loss during the process between the initial mass.[37–39] The experimental details are the following: (i) The activation with CO_2 was carried out in a horizontal reactor where 3 g of CXG were heated at 840 °C in N_2 (heating rate of 10 °C min^{-1}) before flowing CO_2 (flow of 150 $Ncm^3 min^{-1}$) for 120 min.[40] The cooling step was done under N_2 atmosphere. A 15% burn-off was reached with the activation with CO_2. Carbon xerogels so obtained were named as CXG–CO_2. (ii) Water steam activation treatment was carried out in a tube furnace fed by a flow of N_2 saturated with steam. The sample (3 g of CXG) was placed in the oven, and upon reaching 840 °C (in N_2 atmosphere), the N_2 was saturated with boiling water flowing at 1 mL min^{-1} for 90 min.[41] Finally, unsaturated N_2 was passed again to cool the sample. Upon this water vapour activation treatment, the CXG presented an activation degree of 33%. Carbon xerogels activated by water vapour were named as CXG–H_2O. (iii) In the activation with KOH, 3 g of CXG was mixed with KOH pellets in a 2:1 KOH:CXG mass ratio. The mixture was introduced into a stainless-steel reactor and was heated at a rate of 5 °C min^{-1} to 840 °C for one hour under N_2 flow of 150 $Ncm^3 min^{-1}$.[42] Next, the heat-treated material was washed with 1 M HCl and with distilled water until completely neutralization. The percentage of activation obtained was 38%. Chemically activated carbon xerogels were named as CXG–KOH.

Fe–N–CXG synthesis

Fe–N–C catalysts using the different activated carbon xerogels as matrix were synthesized (Fe–N–CXG) upon firstly impregnating CXGs with urea in a 1:10 mass ratio (CXG:urea) and subsequently treating in N_2 for 2 h at 800 °C. These samples are denoted as N–CXG–X, where X corresponds to the activation method (CO_2, H_2O or KOH). Iron acetate, FeAc (95% Sigma-Aldrich), was used as iron precursor. 2 g of N–CXG–X were first dispersed by sonication in deionized water for 10 min. On the other hand, FeAc was dispersed in an ethanol-water solution (1:1, ethanol 96% analytical grade, Labkem) in order to obtain a 1 wt% of Fe nominal loading.[13] Both N–CXG–X and FeAc dispersions were mixed and stirred for 1 h. Then the solution was dried in a vacuum stove, and subsequently grinded in a planetary mill, for 3 h at 400 rpm inside a ZrO_2 vase, sealed in an inert atmosphere. The ball-to-powder mass ratio was 40:1 as in previous works.[43] Finally, the catalyst was pyrolyzed under an N_2 flow for 1 h at 1050 °C followed by fast cooling (quenching). For comparison, a non-activated CXG was also doped with Fe and N following the same procedure previously described. To remove inactive species and create new active ones, several cycles of acid leaching/thermal treatments were performed on each catalyst in order to maximize its catalytic activity. To do so, catalysts were washed with perchloric acid (0.1 M $HClO_4$) for 15 minutes and heated at 950 °C for 1 h in N_2. The number of cycles performed was optimized to obtain the maximum activity towards the ORR for each catalyst. Catalysts will be indicated as Fe–N–CXG–X, where X stands for the activation treatment, CO_2, H_2O or KOH.

Physicochemical characterization

N_2 physisorption at −196 °C (Micromeritics ASAP 2420) was performed to assess the textural properties of the activated carbonaceous materials. The total surface area was determined applying the Brunauer-Emmer-Teller equation (S_{BET}); total pore volume (V_{pore}) was calculated at $P/P^0 = 0.99$ and $V_{mesopore}$ was calculated as described in Zapata-Benabithe et al.[44] The pore size distribution was figured out with the quenched solid density functional theory (QSDFT) assuming a slit-pore geometry.[45] The microporosity of the samples was also evaluated by CO_2 physisorption using the same Micromeritics ASAP 2420 instrument at 0 °C.

Micropore volume ($V_{micropore}$) was obtained by Dubinin-Radushkevich equation and the average pore size (L_0) was calculated by means of Stoeckli and Ballerini equation as described in Fairén-Jiménez et al.[46] The CHNS composition was determined by elemental analysis (EA) in a Thermo Flash 1112 analyser, and the amount of nitrogen and oxygen was also ascertained by X-ray photoelectron spectroscopy (XPS). XPS analyses were performed in an ESCA Plus Omicron spectrometer with an Al (1486.7 eV) anode, using 225 W (15 mA, 15 kV) power. CasaXPS software was employed to fit the XPS peaks. The Fe amount was assessed by atomic emission spectrometry with inductive coupling plasma (ICP-AES) in a Xpectroblue-EOP-TI FMT26 (Spectro) equipment. The crystalline structure of the Fe–N–CXG catalysts was investigated with X-ray diffraction (XRD), in a Bruker AXS D8 Advance diffractometer for polycrystalline powders, Cu Kα source and with a θ-θ configuration.

Electrochemical characterization

Electrochemical measurements were carried out at room temperature in a three-electrode system connected to a microAutolab potentiostat/galvanostat (Metrohm). The reversible hydrogen electrode (RHE) was selected as reference electrode and the counter-electrode was a glassy-carbon rod. The working electrode selected was the rotating disk electrode (RDE) composed of a glassy carbon disk (disk diameter = 5 mm) on top of which an ink containing the catalyst was deposited by drop casting. The ink was prepared from a solution of isopropanol and water (1:3 vol) with 7 mg of the catalyst under study (accounting for 600 $\mu g\,cm^{-2}$ of catalyst loading) and 15 μL of a Nafion® solution (10 wt.% perfluorinated resin dispersion), equivalent to a 15 wt.% of the total catalyst layer. The ORR measurements were conducted in an O_2-saturated 0.5 M H_2SO_4 electrolyte solution and the scan rate of the linear sweep voltammograms was 2 $mV\,s^{-1}$.

The number of exchanged electrons was calculated by means of the Koutecky-Levich method using the following equation (Equation 1):

$$\frac{1}{j}=\frac{1}{j_k}+\frac{1}{j_d}=\frac{1}{j_k}+\frac{1}{0.62nFD_{O_2}^{2/3}v^{-1/6}C_{O_2}\omega^{1/2}} \quad (1)$$

where j is the experimental current density ($mA\,cm^{-2}$), j_d is the diffusion limiting current density ($mA\,cm^{-2}$), and j_k is the kinetic current density ($mA\,cm^{-2}$). The electron transfer number (n) was determined by the linear correlation between the inverse of current density and the inverse of the square root of rotation rate (ω) in rad s^{-1}. F corresponds to the Faraday constant (96,485 $C\,mol^{-1}$), C_{O2} is the concentration of O_2 in the solution (in $mol\,cm^{-3}$), D_{O2} is the diffusion coefficient of O_2 in the electrolyte (1.5×10^{-5} $cm^2\,s^{-1}$),[35] and ν is the kinematic viscosity of 0.5 M H_2SO_4 aqueous solution (1.1×10^{-2} $cm^2\,s^{-1}$).[47]

Fuel cell tests

The Fe–N–C catalysts were tested at the cathode of a polymer electrolyte fuel cell in single cell configuration. An ink solution with the catalyst and Nafion® in isopropyl alcohol was prepared, keeping an ionomer-to-catalyst ratio of 0.82. The ink solution was sonicated for 20 min before being sprayed on a carbon paper (5 cm^2, Sigracet GDL-39BC) to obtain an electrode with a catalyst loading of 4 $mg\,cm^{-2}$ and a percentage of 45 wt.% Nafion®. The anode was prepared in the same way with a commercial Pt/C catalyst (40 wt.% Pt, HiSpec 4000, Alfa Aesar), with a Pt loading of 0.2 $mg\,cm^{-2}$ and 33 wt.% of Nafion®. Both anode, cathode and the membrane (pre-treated Nafion®NR212) were hot-pressed at 25 $kgf\,cm^{-2}$ pressure and 125 °C for 5 min to assemble the membrane-electrode assemblies (MEAs).

The MEAs were placed in a 5 cm^2 single cell equipped with serpentine flow channels at both sides, kept with external heating at 80 °C. The cell temperature was measured close to the flow channel at the cathode side. Fuel cell experiments were performed in a Fuel Cell Technologies Inc. station. The cell was supplied with pre-heated (85 °C) and fully humidified oxygen and hydrogen. The flow rate and the backpressure at the cathode correspond to 1.5 the stoichiometric value and at 150 kPa, respectively. At the anode these values correspond to 1.3 and 130 kPa.

Results and discussion

Physicochemical characterization of carbon xerogels

The textural properties of the non-activated and activated CXGs were studied by both N_2 and CO_2 physisorption experiments. N_2 physisorption isotherms are reported in Figure 1a, whereas CO_2 isotherms are reported in Figure 1b. Both the non-activated and the activated CXGs present a type I isotherm (Figure 1a), associated with microporous solids, with the presence of a slight hysteresis above 0.5 relative pressures, associated with the presence of mesopores. All the activation treatments lead to an increased gas adsorption at low pressures in both the N_2 (Figure 1a) and CO_2 (Figure 1b) isotherms, indicating that the activation treatments increase the microporosity of the original carbon material. This increase is proportional to the activation percentage: the CXG activated by CO_2 (with a 15% of activation percentage) presents fewer micropores than the CXG activated by steam (33%) and the one activated by KOH (38%). The pore size distribution is also presented in Figure 1c. Pore size distribution follows the same trend, CXGs with higher activation percentages showing a higher concentration of micropores than those CXGs with lower activation percentages. Pore size distribution shows a significant peak centered at around 1.3 nm for CXG–H_2O and CXG–KOH, and a much lower and wider contribution between 2.5 and 4.5 nm. On the other hand, CXG–CO_2 shows a significant contribution to pore size below 1 nm, and a lower contribution around 1.3 nm if compared to the other activated samples.

Table 1 summarizes the main textural properties of the carbon xerogels as determined from the nitrogen and carbon dioxide isotherms. In numerous works, activation of CXGs with CO_2[22,25,40] and KOH[42,48–50] is used, obtaining materials with S_{BET} similar to this work. In contrast, there are fewer studies in which activation by water steam is applied.[41,42] Physical activation methods (CO_2 and H_2O) increase the surface area and pore volume of the non-activated carbon material between 1.5 and 2-fold. The highest surface area and pore volume was obtained by chemical activation with KOH (1643 $m^2\,g^{-1}$ and 0.72 $cm^3\,g^{-1}$). This increase is mainly ascribed to the increase of micropore volume, as shown in the isotherms (Figure 1a). The size of the micropores calculated from CO_2 physisorption also widens with the activation methods, especially with the methods characterized by a high percentage of activation (CXG–H_2O and

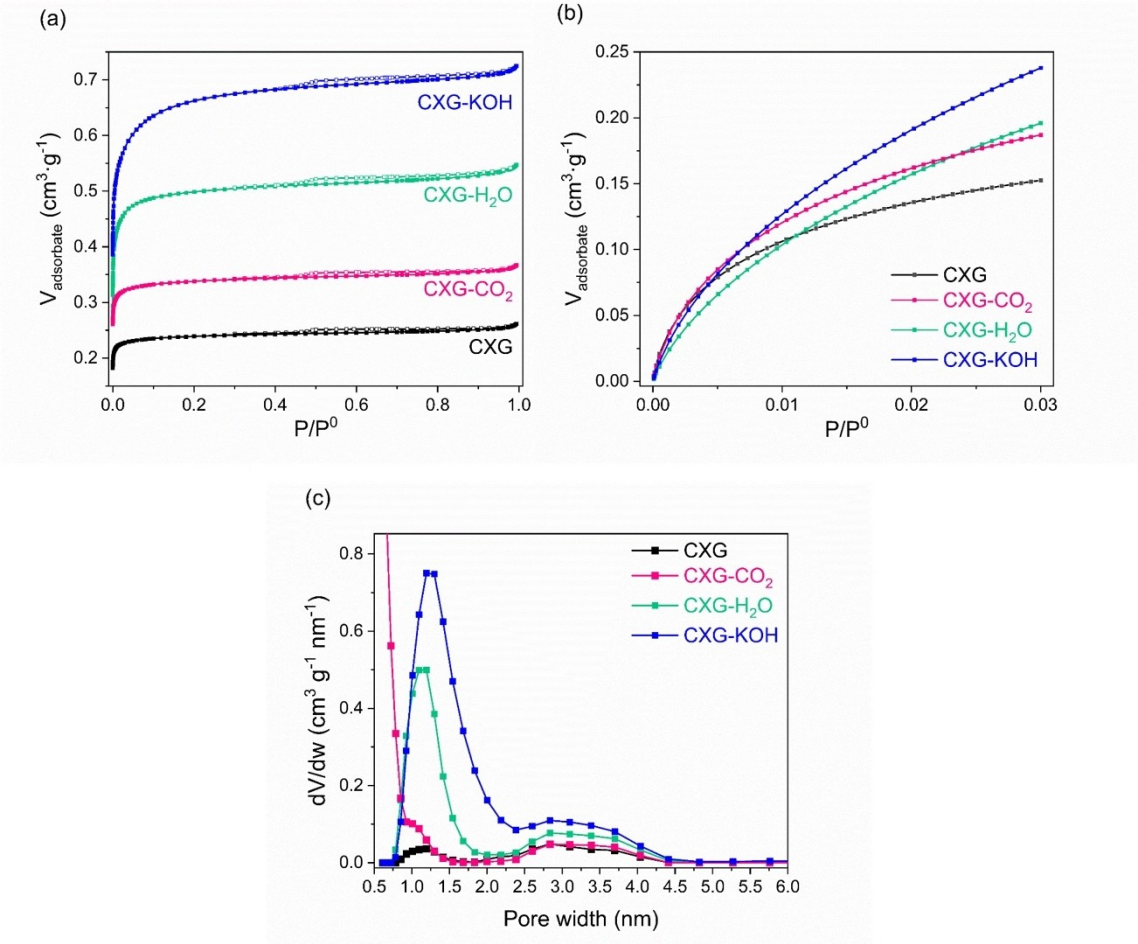

Figure 1. (a) N_2 adsorption/desorption isotherms (full symbols = adsorption, empty symbols = desorption) and (b) CO_2 adsorption isotherms. (c) Pore size distribution obtained from N_2 isotherms.

Table 1. Textural properties determined from N_2 and CO_2 physisorption.

Sample	N_2 physisorption					CO_2 physisorption	
	S_{BET}	V_{pore}	$V_{micropore}$	$V_{mesopore}$	Pore size	$V_{micropore}$	L_0
	$m^2 g^{-1}$	$cm^3 g^{-1}$	$cm^3 g^{-1}$	$cm^3 g^{-1}$	nm	$cm^3 g^{-1}$	nm
CXG	614	0.26	0.23	0.03	1.19	0.29	0.56
CXG–CO_2	893	0.37	0.33	0.04	1.09	0.37	0.62
CXG–H_2O	1267	0.54	0.48	0.06	1.15	0.40	0.72
CXG–KOH	1643	0.72	0.64	0.08	1.25	0.48	0.70

CXG–KOH). Activated CXGs show a slight increase in the mesopore volume, ranging from 0.03 $cm^3 g^{-1}$ for the non-activated CXG up to 0.08 $cm^3 g^{-1}$ representing only a 11% of the total pore volume. In any case, these carbon xerogels are not highly mesoporous. During synthesis at pH 5.2 very small and highly interconnected spheres are formed which do not leave big pores (mesopore size) among them.

The increase of microporosity upon activation with CO_2 is caused by the partial gasification of the carbonaceous material (see Equation S1 in the Supporting Information).[41] This fact produces an opening of narrow micropores and the creation of new ones, which is reflected in the increase of the micropore volume. Activation with water steam involves more reactions (see Equations S2 to S5 in the Supporting Information),[51] with CO_2 as an intermediate product and reactant, producing a more significant enlargement of pores (both micro- and mesopores). On the other hand, the chemical activation with KOH also develops the porosity of the carbon material, producing an increase in both the pore volume and the average size of the smaller pores,[52] due to the parallel steps involved during this treatment and carbon lattice expansion by the metallic K

Table 2. Surface chemistry (oxygen content and oxygen speciation) of activated CXGs determined from XPS O1s.

Properties	CXG	CXG–CO_2	CXG–H_2O	CXG–KOH
O at%	4.9	2.9	1.4	8.1
O=C (quinones) % (530.8 ± 0.2 eV)	15.6	20.4	16.0	18.3
O=C (esters, anhydrides or lactones) % (532.4 ± 0.2 eV)	31.1	29.2	31.5	29.8
O–C (esters, anhydrides) % (533.4 ± 0.2 eV)	27.2	22.7	22.4	22.0
O–C (carboxylic) % (534.5 ± 0.2 eV)	12.4	12.5	11.1	5.7
H_2O (adsorbed) % (536.3 ± 0.2 eV)	13.7	15.1	19.0	24.2

intercalation (see Equations S6 to S14 in the Supporting Information[53]).

The surface chemistry of the activated carbon xerogels was assessed by XPS. Table 2 shows the oxygen content and the oxygen speciation determined from XPS upon deconvolution of the O1s spectra (shown in Figure S1). As previously reported, the bare CXG prior to any activation treatment, presents a surface enriched in oxygen groups (4.9 at% O), with a variety of groups on its surface, mainly esters, anhydrides/lactones, alongside carboxylic and quinone groups.[54] Upon physical activation (CXG–CO_2 and CXG–H_2O), the surface oxygen content decreases (to 1.4–2.9 at% O). This could be attributed to the desorption of labile oxygen groups during activation at high temperature. On the other hand, the chemical activation with KOH causes a certain oxidation of the carbonaceous surface, increasing the oxygen content to 8.1 at%. Compared to bare CXG, the relative amount of quinone/carbonyl groups increases in all the activated carbon materials. Also, the amount of adsorbed water increases with increasing activation degree, meaning that, upon activation, the surface of the carbon material becomes more hydrophilic.

Table 3 shows the deconvolution of the C1s spectra (shown in Figure S2). CXG–KOH presents the largest amount of oxidized carbon species (–C–O and C=O), whereas physically activated CXGs show a similar amount of oxidized carbon species than the non-activated counterpart.

Upon doping with urea of CXG, and before the incorporation of iron, nitrogen concentration reaches 4.5–4.7 wt.% regardless the properties of carbon xerogel. The chemical composition by elemental analysis is summarized in Table S1 of the Supporting Information.

Table 3. Surface chemistry (carbon content and carbon speciation) of activated CXGs determined from XPS C1s.

Properties	CXG	CXG–CO_2	CXG–H_2O	CXG–KOH
C at%	95.1	97.1	98.6	91.9
C sp^2 % (284.6 ± 0.1 eV)	58.2	59.1	61.0	47.7
C sp^3 % (285.3 ± 0.2 eV)	12.6	15.5	14.6	14.2
C–O % (286.3 ± 0.2 eV)	8.8	8.5	7.9	10.2
C=O % (287.5 ± 0.1 eV)	4.7	3.1	2.7	6.0
C π–π^* % (289.4 ± 0.2 eV)	11.0	10.9	12.5	13.8

Table 4. Chemical composition of catalysts determined by ICP and elemental analysis.

Catalyst	ICP (wt.%)	Elemental analysis (wt.%)	
	Fe	C	N
Fe–N–CXG	0.29	95.9	0.62
Fe–N–CXG–CO_2	0.83	92.8	0.95
Fe–N–CXG–H_2O	0.68	92.3	0.98
Fe–N–CXG–KOH	0.35	95.8	0.72

Chemical composition of Fe–N–CXG catalysts

The chemical composition of the Fe–N–CXG catalysts was studied by ICP, EA and XPS (see Table 4 and Table S1 in the Supporting Information). The catalysts based on physically activated CXGs (Fe–N–CXG–CO_2 and Fe–N–CXG–H_2O) and chemically activated CXG (Fe–N–CXG–KOH) present a higher amount of iron (around 0.68–0.83 wt.% and 0.35 wt.%, respectively) than the non-activated counterpart (0.29 wt.%). However, neither the iron nor nitrogen total contents do correlate linearly with the micropore volume. Indeed, CXGs presenting the highest activation degree are not the ones with the highest Fe content. Differences on both nitrogen and iron content in Fe–N–CXG catalysts could be thus ascribed to either differences in the morphology of micropores and/or the influence of the surface chemistry of the carbon material.[55] A significant

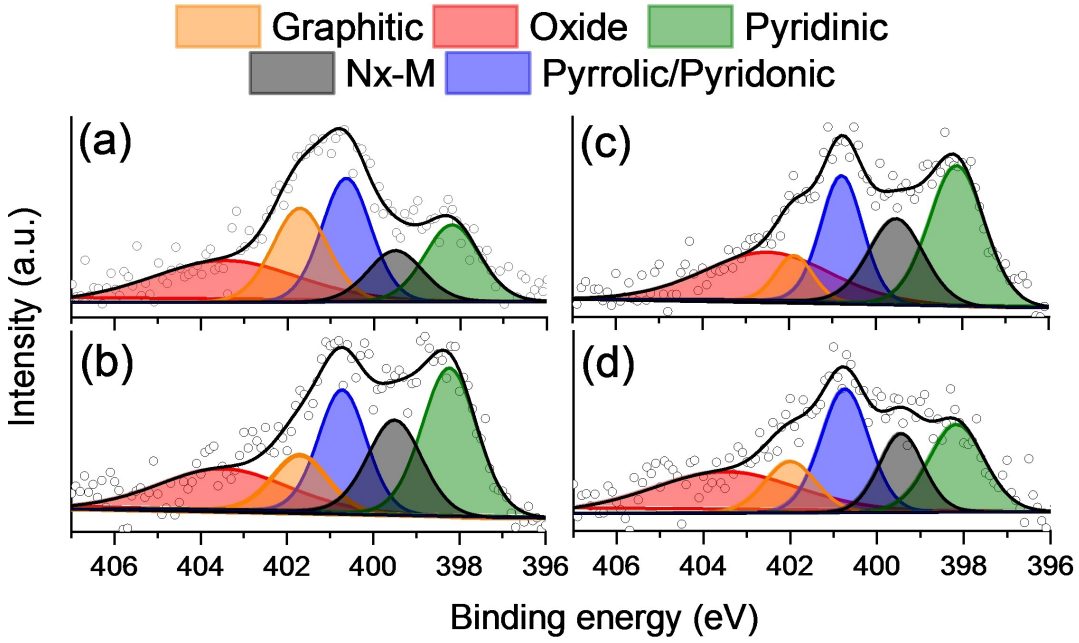

Figure 2. XPS high resolution N1s spectra for (a) Fe–N–CXG, (b) Fe–N–CXG–CO_2 (c) Fe–N–CXG–H_2O and (d) Fe–N–CXG–KOH.

increase of pore volume but with similar or slightly larger micropore sizes indicates deeper pores upon activation. This aspect could negatively influence the uptake of iron precursor. Moreover, catalysts on CXGs with a larger oxygen content (Fe–N–CXG and Fe–N–CXG–KOH), show a lower Fe content, also indicating a negative influence of oxygen surface groups on the anchorage of the iron precursor. Bandosz et al. reported that pre-oxidized samples treated with urea presented lower oxygen contents after heat-treatment, due to the kind of chemical bonds formed between oxygen species and urea, leading to thermally unstable species.[55] Since Fe is introduced in the carbon matrix after nitrogen doping, the absence or presence of certain oxygen groups could determine how much iron is anchored to the carbon matrix. In fact, catalysts based on activated CXGs show a lower amount of oxygen compared to Fe–N–CXG (see Table S1 in the Supporting Information), what justifies the loss of oxygen groups upon nitrogen doping at high temperature.

In Fe–N–C catalysts synthesized from carbon materials, a relevant plurality of active sites can be found originated from both Fe-containing species like single atom sites (e.g. Fe–N_x where x is the number of nitrogen atoms coordinated with one Fe atom, typically between 2 and 5), including the possible formation of Fe-based nanoparticles (magnetic Fe_α, Fe_γ, nitrides or carbides), and also Fe-free moieties, mostly nitrogen species (pyridinic, pyridonic, etc.).[56] It has been previously reported that Fe–N_x active sites are usually hosted in the micropores, in particular those with size between 1 and 2 nm.[57–59]

The high-resolution N1s XPS spectra for Fe–N–C catalysts were deconvoluted into five peaks as: pyridinic N (398.2 ± 0.1 eV), N_x–M (399.5 ± 0.1 eV), pyrrolic N (400.7 ± 0.2 eV), graphitic N (401.8 ± 0.2 eV), and oxidized N (403 ± 0.3 eV).[60] Pyrrolic and pyridinic N correspond to nitrogen atoms incorporated in five- and six-membered heterocyclic aromatic rings, respectively,[61] while N_x–M refers to nitrogen coordinated to metallic atoms (iron in this case).[62,63] Figure 2 shows the deconvoluted XPS spectra for the N1s orbital of the Fe–N–C catalysts and Table 5 shows the chemical speciation for nitrogen.

Catalysts obtained with activated CXGs present a larger amount of N_x-Fe functionalities (ranging from 0.15 at% to 0.21 at%) compared to the non-activated counterpart (0.09 at %). Besides, pyridinic nitrogen is also present in a higher concentration in those catalysts coming from activated samples, ranging from 0.20 to 0.33 at%, compared to 0.13 at% for Fe–N–CXG. Pyridinic N is fundamental for the 2×2 e^- mecha-

Table 5. Chemical speciation (total atomic %) from the N1s orbital XPS analysis.

Sample	N-Pyridinic (N6)	N_x–M	N-Pyrrolic (N5)	N-Graphitic	N-oxide	Ratio N6/N5
Fe–N–CXG	0.13	0.09	0.19	0.16	0.19	0.68
Fe–N–CXG–CO_2	0.33	0.21	0.24	0.12	0.21	1.38
Fe–N–CXG–H_2O	0.30	0.18	0.21	0.07	0.24	1.43
Fe–N–CXG–KOH	0.20	0.15	0.25	0.11	0.25	0.80

nism of the oxygen reduction reaction. In the case of the Fe–N–CXG–KOH catalyst, despite the substantial rise of surface area and micropore volume upon chemical activation, the amount of N-pyridinic and N_x–M does not increase proportionally. This could be due to the particular surface chemistry created upon KOH activation, that might be preventing the formation of Fe–N active sites.[49,52,64]

Another important parameter to take into account in terms of catalytic activity is the ratio of pyridinic to pyrrolic (or pyridonic) nitrogen (N6/N5). It has been reported in literature that the amount of pyridinic nitrogen with respect to pyrrolic nitrogen (N6/N5) is an indirect measure of the foreseeable catalytic activity of Fe–N–C catalysts.[56,65] The higher the amount of N6 (higher N6/N5 ratio) entails a more efficient ORR, and so, a higher intrinsic activity. This ratio is maximized for catalysts based on physically activated CXGs, *i.e.* Fe–N–CXG–CO_2 and, Fe–N–CXG–H_2O.

Figure 3 shows the XRD patterns of the Fe–N–CXG catalysts. All the samples present two broad peaks ascribed to graphenic carbon at Bragg angles of $2\theta = 26.3°$ and 42–44° assigned to (0 0 2) and (1 0) reflections, respectively (JCPDS No. 41-1487).[66,67] The width and intensity of these peaks, especially the peak at 26°, are related to the ordering degree of the carbon material. Fe–N–CXGs obtained on activated CXGs show a broader peak at 26°, which indicates a smaller size of crystallites or lattice defects.[49,64] From the magnified view (Figure 3, right), the XRD pattern of Fe–N–CXG exhibits peaks ascribed to metallic iron, Fe_α (JCPDS No. 01-087-0721) located at $2\theta = 44.8°$, 65.5° and 82.6°.[68] However, these peaks disappear in the samples activated with CO_2 and H_2O, but it is still present for Fe–N–CXG–KOH, although with a broader and less intense reflection. Fe_γ (JCPDS No. 99-900-8470) is also present in physically activated samples, with peaks at $2\theta = 43.8°$, 51° and 74.9°, indicating the presence of Fe_γ. Both phases (Fe_γ and Fe_α) do not present activity towards the ORR.[68]

The presence of metallic Fe phases on all the catalysts, alongside the existence of Fe–N_x sites, as determined by XPS, reveal that two phenomena might be taking place upon iron doping. Fe is probably anchoring on both surface oxygen groups, as metallic iron, and on N–C sites, as Fe–N_x–C. Ma and collaborators reported that, upon activation of carbon materials with CO_2, there is a decrease of metallic phases if compared to bare carbon, as it occurs in our study.[69] They ascribed that the increased porosity of the activated samples could lead to high dispersion of doped Fe atoms, avoiding the interaction of iron with the bare carbon matrix.

Activity of Fe–N–CXG towards the oxygen reduction reaction in acidic medium

The activity towards the oxygen reduction reaction (ORR) of the Fe–N–CXG–X catalysts, where X represents the activation method (CO_2, H_2O or KOH), was evaluated in a rotating disk electrode in 0.5 M H_2SO_4 aqueous electrolyte. Figure 4 shows the linear sweep voltammetries for the Fe–N–CXG–X catalysts. Before analysing the effect of CXG activation, the influence of acid leaching and thermal treatment was evaluated. Fe–N–C

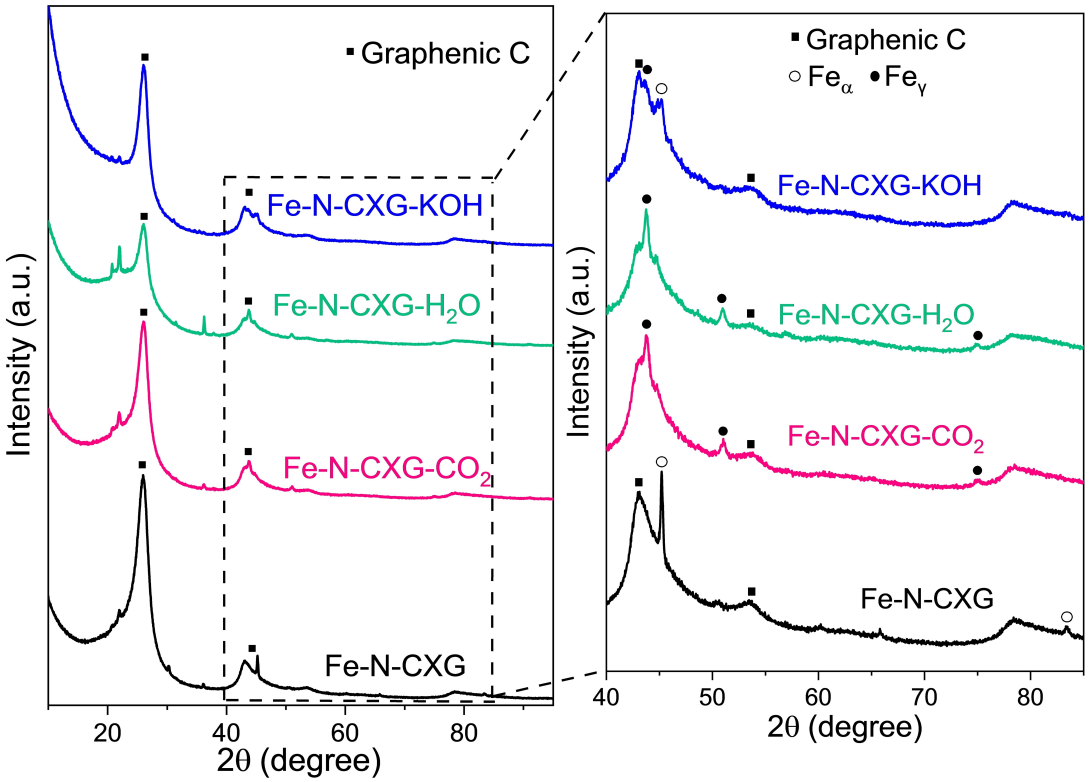

Figure 3. XRD patterns for Fe–N–CXG, Fe–N–CXG–CO_2, Fe–N–CXG–H_2O and Fe–N–CXG–KOH. Graph at the right shows the diffractogram at the left zoomed from 40 to 80 degrees, for the sake of a better peak visualization.

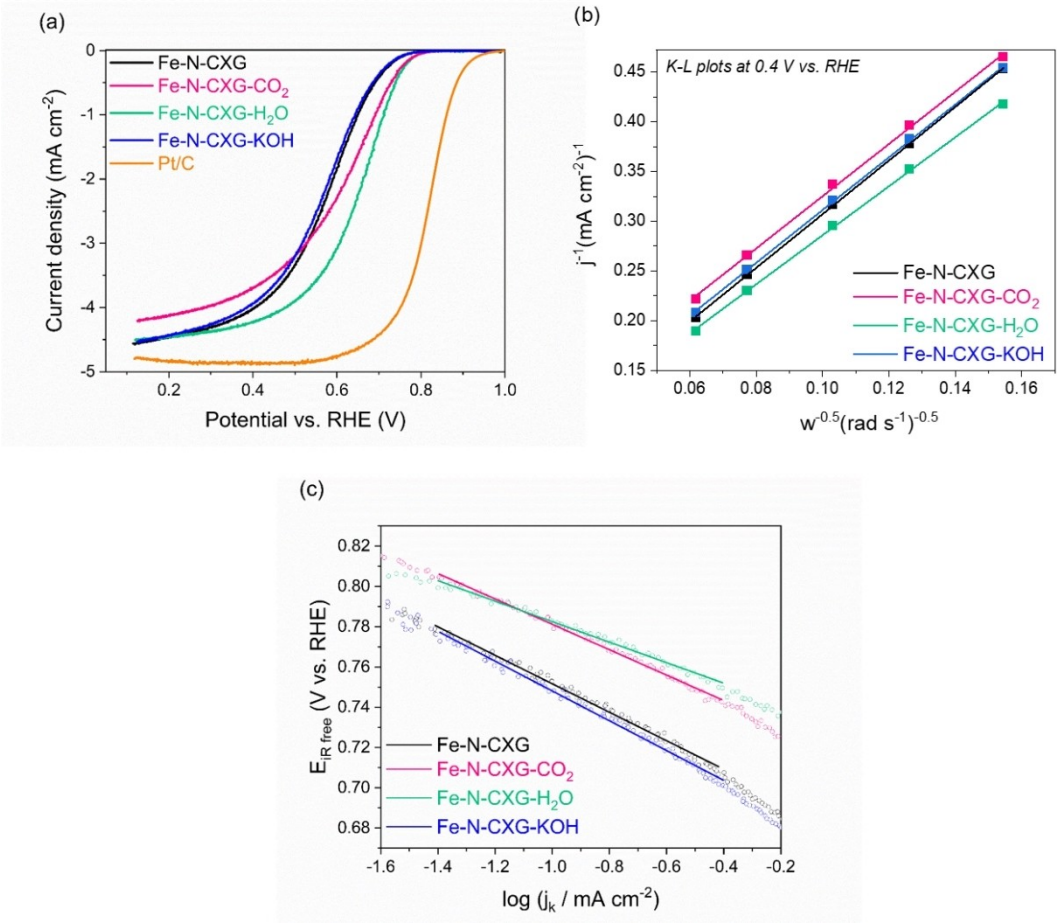

Figure 4. (a) Polarization curves for the ORR in RDE at 1600 rpm in O_2-saturated 0.5 M H_2SO_4. **(b)** Koutecky-Levich diagrams obtained at 0.4 V vs. RHE; **(c)** Tafel plot from LSV at 1600 rpm for the ORR.

catalysts were subjected to several cycles of acid leaching/thermal treatments (AL/TT) to remove inactive and unstable Fe particles, favouring the creation of new active sites.[28,68] The effect of acid-thermal treatment on the electrocatalytic activity of the catalysts towards the ORR was assessed (see Figure S3 of the Supporting Information). A similar trend is observed in all catalysts, after the first AL/TT cycle the activity of the catalyst improves substantially. However, after a certain number of cycles, activity decreases due to an excessive removal of iron and the loss of conductivity, as previously reported.[70,71] Therefore, there is an optimal number of AL/TT cycles for each catalyst to maximize its catalytic activity. The number of cycles needed to maximize the activity is not the same for all the catalysts presented in this work, since it depends on the porosity and the surface chemistry of the catalyst. Catalysts shown in Figure 4 are those with the optimal number of cycles giving rise to the maximum ORR activity. Further details can be found in the Supporting Information (Figure S3). The physicochemical characterisation presented above is also carried out on Fe–N–CXG catalysts with the optimum number of cycles.

Table 6 provides the main electrochemical parameters: the onset potential (E_{onset}) recorded at −0.1 mA cm^{-2}, the half-wave potential ($E_{1/2}$), the number of exchanged electrons (n) and the Tafel slope. The use of physically activated xerogels (CXG–CO_2 and CXG–H_2O) in the synthesis of Fe–N–C catalysts significantly improves their activity against ORR in terms of E_{onset} (by 30 mV) and $E_{1/2}$ (by 40–80 mV). As previously stated, these catalysts were those with the highest amount of N_x–Fe sites and pyridinic nitrogen, alongside the highest N6/N5 ratio (Npyridinic/Npyrrolic).[72] Therefore, the improvement in activity in this case is related to a higher percentage of the cited species that effectively catalyze ORR. N6/N5 ratio for these catalysts shows the following order: Fe–N–CXG–CO_2 (1.38) <

Table 6. Electrochemical parameters for the Fe–N–CXG catalysts. Potentials are referred versus the RHE. *n* refers to the number of electrons exchanged calculated from Koutecky-Levich diagrams obtained at 0.4 V vs. RHE.

Catalyst	E_{onset} V_{RHE}	$E_{1/2}$ V_{RHE}	n	Tafel slope mV dec^{-1}
Fe–N–CXG	0.75	0.57	3.6	71
Fe–N–CXG–CO_2	0.78	0.61	3.7	63
Fe–N–CXG–H_2O	0.78	0.65	4.0	51
Fe–N–CXG–KOH	0.75	0.57	3.7	74
Pt/C	0.94	0.82	4.0	61

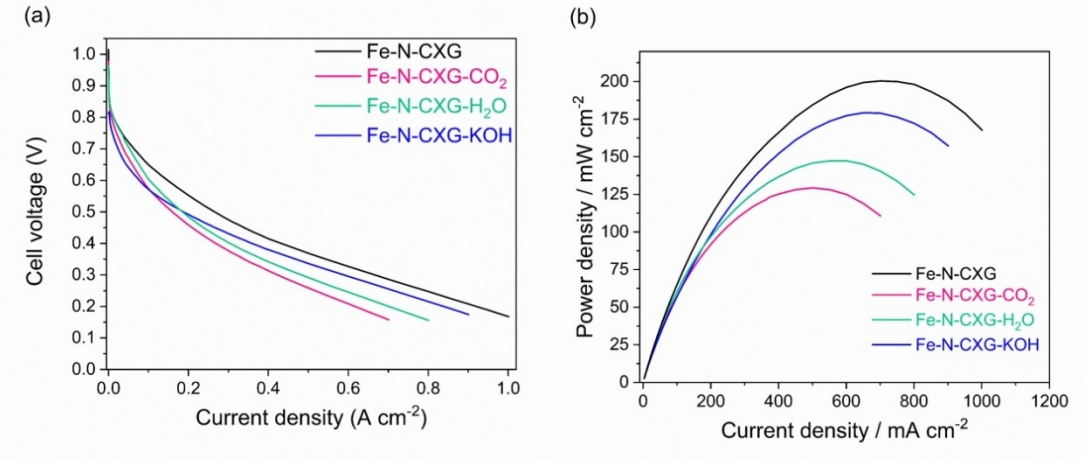

Figure 5. (a) Polarization curves and **(b)** power density curves for MEAs comprising cathodes made with Fe–N–CXG catalysts (4 mg cm^{-2}), Nafion® NR212 membrane, and $Pt_{40\%}$/C (0.2 mg_{Pt} cm^{-2}) at the anode. Operating conditions: 80 °C; H_2/O_2 at λ = 1.3/1.5, 100 % RH, and back pressure of 1.5 bar-gauge.

Fe–N–CXG–H_2O (1.43), correlating well with the catalytic activity. On the other hand, the chemical activation of CXG with KOH does not lead to an improvement in the catalytic activity, as this catalyst presented a lower Fe iron content and N6/N5 ratio than the other activated counterparts.

As evidenced, these catalysts present an ORR activity lower than the state-of-the-art Fe–N–C catalysts.[3,68,73,74] This might be due to the low N content, causing a low density of active sites if compared to template-based procedures with coordinated iron precursors. However, it must be taken into account that the Fe–N–CXG catalysts of this work were obtained by a template-free method, which is more sustainable and which has room for improvement, since N-doped carbon xerogels can be obtained with a great variety of precursors, providing a higher amount of N. Moreover, the scope of this work is to evaluate the effect of the activation treatment of the carbon material on the ORR activity. The catalytic activity could be further improved by post-treatment with NH_3, in order to promote the creation of new active sites.

The number of exchanged electrons (calculated by applying the K–L equation from data plotted in Figure 4b) in the catalysts ranges between 3.6 and 4, indicating that a high percentage of sites follow the 2x2- or the 4-electron mechanism. Artyushkova et al. conducted a study of 45 electrocatalysts obtained by different methods and concluded that pyridinic nitrogen participates in the reduction of H_2O_2 to H_2O.[65,68] Therefore, it appears that the presence of pyridinic nitrogen in our set of catalysts is related to the increase in the number of exchanged electrons in the oxygen reduction reaction.

The analysis of the Tafel plot, giving information on the reaction kinetics, is presented in Figure 4c. The catalysts synthesized with physically activated CXG (Fe–N–CXG–H_2O and Fe–N–CXG–CO_2) present a lower Tafel slope (51 and 63 mV dec^{-1}, respectively) in comparison with the non-activated based catalyst (Fe–N–CXG, 71 mV dec^{-1}) and the chemically activated one (Fe–N–CXG–KOH, 74 mV dec^{-1}). Lower values of Tafel slope indicate that the ORR proceeds through a more effective pathway, due to changes in the rate determining step.

Activity and stability of Fe–N–CXG in fuel cell

Figure 5 depicts the performance of all the studied catalysts at the cathode of a single fuel cell equipped with Nafion® membrane. Table 7, collects the main parameters obtained from the voltage-current curves. Firstly, it is noticeable that the activity trend for Fe–N–CXG catalysts in the full cell does not fully match to the one determined in the half-cell studies. As revealed in Figure 5a, at low current density (activation region),

Table 7. Electrochemical parameters for the Fe–N–CXG catalysts obtained from I–E curves in single cell configuration. Beginning of test (BoT) and end of test (EoT) values as determined before and after the test at constant voltage of 0.5 V.

Catalyst	OCV	Current density @ 0.8 V [(a)]	Mass activity @ 0.8 V[(a)]	Max. power density BoT/EoT	Current loss after 20 h at 0.5 V [(b)]	Max. power dens. loss after 20 h at 0.5 V
	V	mA cm^{-2}	A g^{-1}	mW cm^{-2}	(%)	(%)
Fe–N–CXG	1.02	12.6	3.2	200 / 125	60	37.5
Fe–N–CXG–CO_2	0.98	7.2	1.8	129 / 106	52	17.8
Fe–N–CXG–H_2O	0.97	12.2	3.1	147 / 100	56	31.9
Fe–N–CXG–KOH	0.81	2.5	0.6	179 / 125	63	30.9

(a) Voltage is not iR corrected, values at BoT, (b) Current loss for chronoamperometric tests.

the catalyst based on the non-activated carbon xerogel (Fe–N–CXG) shows the highest performance, followed closely by the catalyst based on the carbon xerogel activated with water steam (Fe–N–CXG–H_2O). Similar values of current density at 0.8 V were found for these two catalysts (see Table 7), notwithstanding the intrinsic activity evaluated in half-cell configuration was significantly higher for Fe–N–CXG–H_2O. These results highlight the importance of testing catalysts in a fuel cell device, since the electrochemical characterization in RDE offers information on the intrinsic activity of the catalysts with oxygen dissolved in an aqueous electrolyte. Whereas, single cell experiments are carried out with humidified gases under conditions more similar to practical application.

The open circuit voltage (OCV) is 1.02 V, 0.98 V and 0.97 V for Fe–N–CXG, Fe–N–CXG–CO_2 and Fe–N–CXG–H_2O, respectively. These values are higher than the OCVs recently obtained for Fe–N–C catalysts based on carbon gels (0.85 V).[75] On the contrary, Fe–N–CXG–KOH shows a lower value of OCV of 0.81 V, but a better behavior at high current densities. This might be due to its larger porosity and slightly higher mesopore volume that could favor mass transfer processes. A commercial Pt/C catalyst was also tested under the same conditions, see Figure S4, and the OCV value is 0.96 V, in line with typical values in the literature and comparable to the OCV values for the MEAs equipped with Fe–N–CXG.

Fe–N–CXG presents a maximum value of power density of 200 mW cm^{-2} (Figure 5b and Table 7), superior to other Fe–N–C catalysts in the literature obtained from similar carbon materials. Kicínski et al. reported Fe–N–C catalysts synthesised by the sol-gel process with a maximum power density value of 135 mW cm^{-2}.[75] Other Fe–N–C catalysts based on aerogels presented a similar maximum power density value after optimization of the ink and with a back pressure of 1.5 bar, like the experiments of this work.[68]

Several studies on literature have reported the influence of important variables on the catalytic performance, such as the MEA assembly conditions, the ink recipe, the texture and thickness of the catalytic layer, and the degree of hydrophobicity. All these electrode parameters must be taken into account since they determine the accessibility to active sites of the catalyst, and other important issues such as electrode flooding conditions in a fuel cell.[76]

To assess the differences arising from the different electrode structure, the degree of hydrophobicity of the electrodes was evaluated by depositing a drop of water on the surface of a fresh electrode (Figure S5). Fe–N–CXG presents a higher degree of hydrophobicity compared to the activated counterparts, which contributes to a better water evacuation, diminishing the effect of flooding from the water produced during operation and eventually, leading to a better activity in fuel cell.[77] In fact, it has been recently reported that hydrophilic Fe–N–C cathodes have shown poorer performances due to an excessive water saturation, reducing the access to active sites.[78]

Due to the low volumetric activity of PGM-free catalysts, there are very recent studies claiming that the catalytic layer of these electrodes is substantially thick, what implies suffering from poor water management and increased transport resistance, limiting the fuel cell performance. Kim et al. stablished that electrodes based on non-PGM catalysts, that are much thicker than Pt-based catalysts, require an optimization of the electrode composition, in order to avoid transport losses.[79] Besides, it has been also pointed out that most studies assessing PGM-free electrode performance in fuel cells use fully humidified O_2/air to maximize the proton conductivity. However, fully humidified inlet gas makes non-PGM electrodes more prone to water flooding, what eventually can cause a long-term performance degradation.[79] In order to improve the performance of catalysts with a high hydrophilicity, careful attention should be paid to the MEAs assembling process. Since this is a very recent field of study, the present electrodes have a great room of improvement in order to be tested in the best conditions, but this is not the scope of the present manuscript. Future studies will take all these new studies in consideration prior to MEA testing. Some of the strategies recently reported to improve fuel cell performance include using catalyst-coated membranes (instead of gas-diffusion-layers), cold-pressing or improved hot-pressing procedures.[78]

The long-term stability and durability of Fe–N–C catalysts in PEFC still remains a real challenge.[80–82] In order to assess the stability of the catalysts, MEAs were also subjected to a durability test consisting of 20 h operation at 0.5 V (Figure 6). The polarization curves and power density curves at the end of test (EoT) are exhibited in Figure S6 and the comparison of parameters with respect to the beginning of test (BoT) is summarized in Table 7.

After the durability test, the current density of the catalysts decreases around 52–63 %. Most of the current decay occurs at the first hours of the test. Kicinski and co-workers also studied the durability of Fe–N carbon gel catalysts for 50 h at 0.5 V.[75] They concluded that most of the degradation of the activity occurs at high current densities and in the first hours of operation, after 24 h a current density of approximately 60 %

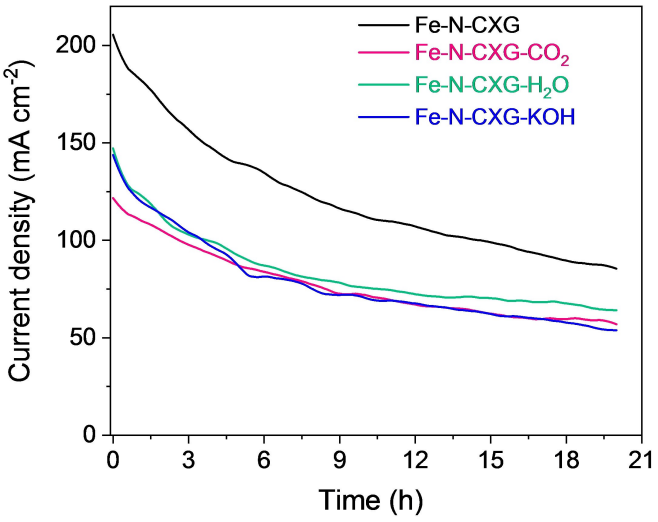

Figure 6. Durability tests: potential holding at 0.5 V for 20 h. Fe–N–CXG catalysts (4 mg cm^{-2}) at the cathode, Nafion® NR212 membrane, and $Pt_{40\%}$/C (0.2 mg_{Pt} cm^{-2}) at the anode. Operating conditions: 80 °C; H_2/O_2 at $\lambda = 1.3/1.5$, 100 % RH, and back pressure of 1.5 bar-gauge.

lower than the initial value was reached. In this regard, the details surrounding degradation mechanisms are active areas of debate in the literature.[5,83] The primary degradation mechanisms for PGM-free catalysts are: (1) demetallation, (2) carbon oxidation, (3) micropore flooding and (4) active-site protonation and anion adsorption,[84] but the main mechanism is not yet clarified.[85] Interestingly, in this work we found that the activation of carbon xerogels is a positive strategy to ameliorate the loss of performance: the catalysts on activated CXGs withstand better the degradation phenomena, showing between 18 and 32% power density loss, which is lower if compared to the catalyst on non-activated CXG, with 37% loss. The highest power density retention was shown by Fe–N–CXG–CO_2 catalyst, with only 17.8% loss. This is the catalyst with the largest content of iron of the series, which may be a parameter influencing the extent of degradation related to metallic species (loss of performance through demetallation).

Conclusions

In this work, activated carbon xerogels co-doped with nitrogen and iron were studied as Fe–N–CXG catalysts for PEMFC. Catalysts were obtained by a template-free alternative to those used to date, by means of a non-polluting, economic and easily optimisable method. With the aim of increasing the amount of active sites, carbon xerogels were activated by both physical (CO_2 and water steam) and chemical (KOH) methods, aimed at increasing microporosity of the carbon matrix. Although a significant increase of the micropore volume is obtained upon activation (the higher the activation degree, the higher the micropore relative content), this is not directly translated into an enhancement of the catalytic activity against the ORR. Chemical activation with KOH produces a high increase of surface area and micropore volume, but at the expense of a surface chemistry hindering the anchorage of N and Fe, leading to a decreased ORR activity. Physical activation methods, with a milder increase of surface area and pore volume, present larger extent of N and Fe incorporation, in particular in the most active forms, pyridinic N and N bonded to metal (Fe), reflected in an enhanced intrinsic catalytic activity. However, despite the increase of intrinsic activity correlated to the increase of micropore content for physically activated carbons, an excessive hydrophilicity is a drawback in a full cell configuration due to excessive flooding. Strategies to facilitate the removal of water are therefore required together with the optimization of pore structure and chemical composition.

Acknowledgements

The authors wish to acknowledge the grant PID2020-115848RB-C21 funded by MCIN/AEI/10.13039/501100011033. This research has received funding from the European Institute of Innovation and Technology (EIT) through project EIT RM – n. 18252. Authors also acknowledge *Gobierno de Aragón* (DGA) for the financial support to *Grupo de Conversión de Combustibles* (T06_23R). L. Álvarez acknowledges also DGA for her pre-doctoral contract.

Conflict of Interests

The authors declare no conflict of interest.

Data Availability Statement

The data that support the findings of this study are available from the corresponding author upon reasonable request.

Keywords: activation · carbon xerogels · Fe–N–C catalysts · microporosity · oxygen reduction reaction

[1] U. Martinez, S. Komini Babu, E. F. Holby, H. T. Chung, X. Yin, P. Zelenay, *Adv. Mater.* **2019**, *31*, 1806545.
[2] Y. Wang, L. Wang, H. Fu, *Sci. China Mater.* **2022**, *65*, 1701–1722.
[3] Y. He, G. Wu, *Acc Mater Res* **2022**, *3*, 224–236.
[4] Y. Qu, W. Zhang, D. Li, H. Yang, Y. Xiao, Y. Liu, *ChemElectroChem* **2022**, *9*, e202101464.
[5] L. Osmieri, J. Park, D. A. Cullen, P. Zelenay, D. J. Myers, K. C. Neyerlin, *Curr. Opin. Electrochem.* **2021**, *25*, 100627.
[6] M. Liu, L. Wang, K. Zhao, S. Shi, Q. Shao, L. Zhang, X. Sun, Y. Zhao, J. Zhang, *Energy Environ. Sci.* **2019**, *12*, 2890–2923.
[7] S. Juvanen, A. Sarapuu, S. Vlassov, M. Kook, V. Kisand, M. Käärik, A. Treshchalov, J. Aruväli, J. Kozlova, A. Tamm, J. Leis, K. Tammeveski, *ChemElectroChem* **2021**, *8*, 2288–2297.
[8] M. J. Workman, A. Serov, L. K. Tsui, P. Atanassov, K. Artyushkova, *ACS Energy Lett.* **2017**, *2*, 1489–1493.
[9] A. Serov, M. J. Workman, K. Artyushkova, P. Atanassov, G. McCool, S. McKinney, H. Romero, B. Halevi, T. Stephenson, *J. Power Sources* **2016**, *327*, 557–564.
[10] A. Zitolo, V. Goellner, V. Armel, M. T. Sougrati, T. Mineva, L. Stievano, E. Fonda, F. Jaouen, *Nat. Mater.* **2015**, *14*, 937–942.
[11] K. Qin, Z. Zhu, F.-X. Ma, J. Zhang, *J. Electroanal. Chem.* **2022**, *906*, 116021.
[12] Q. Jia, N. Ramaswamy, U. Tylus, K. Strickland, J. Li, A. Serov, K. Artyushkova, P. Atanassov, J. Anibal, C. Gumeci, S. C. Barton, M. T. Sougrati, F. Jaouen, B. Halevi, S. Mukerjee, *Nano Energy* **2016**, *29*, 65–82.
[13] E. Proietti, F. Jaouen, M. Lefèvre, N. Larouche, J. Tian, J. Herranz, J. P. Dodelet, *Nat. Commun.* **2011**, *2*, 416.
[14] W. da S. Freitas, A. D'Epifanio, V. C. A. Ficca, E. Placidi, F. Arciprete, B. Mecheri, *Electrochim. Acta* **2021**, *391*, 138899.
[15] R. Sibul, E. Kibena-Põldsepp, S. Ratso, M. Kook, M. T. Sougrati, M. Käärik, M. Merisalu, J. Aruväli, P. Paiste, A. Treshchalov, J. Leis, V. Kisand, V. Sammelselg, S. Holdcroft, F. Jaouen, K. Tammeveski, *ChemElectroChem* **2020**, *7*, 1739–1747.
[16] J. Li, S. Ghoshal, W. Liang, M. T. Sougrati, F. Jaouen, B. Halevi, S. McKinney, G. McCool, C. Ma, X. Yuan, Z. F. Ma, S. Mukerjee, Q. Jia, *Energy Environ. Sci.* **2016**, *9*, 2418–2432.
[17] W. da Silva Freitas, B. Mecheri, C. Lo Vecchio, I. Gatto, V. Baglio, V. C. A. Ficca, A. Patra, E. Placidi, A. D'Epifanio, *J. Power Sources* **2022**, *550*, 232135.
[18] S. Pérez-Rodríguez, D. Sebastián, C. Alegre, T. Tsoncheva, N. Petrov, D. Paneva, M. J. Lázaro, *Electrochim. Acta* **2021**, *387*, 138490.
[19] S. Zago, M. Bartoli, M. Muhyuddin, G. M. Vanacore, P. Jagdale, A. Tagliaferro, C. Santoro, S. Specchia, *Electrochim. Acta* **2022**, *412*, 140128.
[20] C. Alegre, M. E. Gálvez, E. Baquedano, R. Moliner, E. Pastor, M. J. Lázaro, *Cienc. e Tecnol. dos Mater.* **2012**, *24*, 172–175.
[21] N. Rey-Raap, J. Angel Menéndez, A. Arenillas, *Microporous Mesoporous Mater.* **2014**, *195*, 266–275.
[22] M. L. C. Piedboeuf, A. F. Léonard, G. Reichenauer, C. Balzer, N. Job, *Microporous Mesoporous Mater.* **2019**, *275*, 278–287.

[23] M. S. Contreras, C. A. Páez, L. Zubizarreta, A. Léonard, S. Blacher, C. G. Olivera-Fuentes, A. Arenillas, J. P. Pirard, N. Job, *Carbon N Y* **2010**, *48*, 3157–3168.
[24] M. Canal-Rodríguez, A. Arenillas, N. Rey-Raap, G. Ramos-Fernández, I. Martín-Gullón, J. A. Menéndez, *Carbon N Y* **2017**, *118*, 291–298.
[25] M. Canal-Rodríguez, N. Rey-Raap, J. Á. Menéndez, M. A. Montes-Morán, J. L. Figueiredo, M. F. R. Pereira, A. Arenillas, *Microporous Mesoporous Mater.* **2020**, *293*, DOI 10.1016/j.micromeso.2019.109811.
[26] C. Alegre, D. Sebastián, M. E. Gálvez, E. Baquedano, R. Moliner, A. S. Aricò, V. Baglio, M. J. Lázaro, *Materials* **2017**, *10*, 1092.
[27] H. Jin, J. Li, F. Chen, L. Gao, H. Zhang, D. Liu, Q. Liu, *Electrochim. Acta* **2016**, *222*, 438–445.
[28] L. Osmieri, L. Pezzolato, S. Specchia, *Curr. Opin. Electrochem.* **2018**, *9*, 240–256.
[29] H. Zhang, L. Osmieri, J. H. Park, H. T. Chung, D. A. Cullen, K. C. Neyerlin, D. J. Myers, P. Zelenay, *Nat. Catal.* **2022**, *5*, 455–462.
[30] K. Artyushkova, S. Rojas-Carbonell, C. Santoro, E. Weiler, A. Serov, R. Awais, R. R. Gokhale, P. Atanassov, *ACS Appl. Energ. Mater.* **2019**, *2*, 5406–5418.
[31] V. A. Saveleva, K. Kumar, P. Theis, N. S. Salas, U. I. Kramm, F. Jaouen, F. Maillard, P. Glatzel, *ACS Appl. Energ. Mater.* **2023**, *6*, 611–616.
[32] C. Alegre, D. Sebastián, M. Gálvez, E. Baquedano, R. Moliner, A. Aricò, V. Baglio, M. Lázaro, *Materials.* **2017**, *10*, 1092.
[33] H. F. Gorgulho, F. Gonçalves, M. F. R. Pereira, J. L. Figueiredo, *Carbon N Y* **2009**, *47*, 2032–2039.
[34] N. Rey-Raap, J. Angel Menéndez, A. Arenillas, *Carbon N Y* **2014**, *78*, 490–499.
[35] C. Alegre, E. Baquedano, M. E. Galvez, R. Moliner, M. J. Lazaro, *Int. J. Hydrogen Energy* **2015**, *40*, 14736–14745.
[36] P. Bettotti, *Submicron Porous Materials*, Springer International Publishing, **2017**.
[37] P. Feng, J. Li, H. Wang, Z. Xu, *ACS Omega* **2020**, *5*, 24064–24072.
[38] C. F. Chang, C. Y. Chang, W. T. Tsai, *J. Colloid Interface Sci.* **2000**, *232*, 45–49.
[39] H. Mash, F. Rodríguez Reinoso, *Activated Carbon*, Editor: Elsevier, **2006**, ISBN 978-0-08-044463-5.
[40] J. F. Vivo-Vilches, A. F. Pérez-Cadenas, F. J. Maldonado-Hódar, F. Carrasco-Marín, C. Siquet, A. M. Ribeiro, A. F. P. Ferreira, A. E. Rodrigues, *Microporous Mesoporous Mater.* **2018**, *270*, 161–167.
[41] M. Mazzucato, G. Daniel, A. Mehmood, T. Kosmala, G. Granozzi, A. Kucernak, C. Durante, *Appl. Catal. B* **2021**, *291*, DOI 10.1016/j.apcatb.2021.120068.
[42] C. Moreno-Castilla, H. García-Rosero, F. Carrasco-Marín, *Colloids Surf. A* **2017**, *520*, 488–496.
[43] L. Álvarez-Manuel, C. Alegre, D. Sebastián, A. Eizaguerri, P. F. Napal, M. J. Lázaro, *Catal. Today* **2023**, *418*, 114067.
[44] Z. Zapata-Benabithe, F. Carrasco-Marín, J. De Vicente, C. Moreno-Castilla, *Langmuir* **2013**, *29*, 6166–6173.
[45] A. V. Neimark, Y. Lin, P. I. Ravikovitch, M. Thommes, *Carbon N Y* **2009**, *47*, 1617–1628.
[46] D. Fairén-Jiménez, F. Carrasco-Marín, D. Djurado, F. Bley, F. Ehrburger-Dolle, C. Moreno-Castilla, *J. Phys. Chem. B* **2006**, *110*, 8681–8688.
[47] A. J. Bard, G. Inzelt, F. Scholz, *Electrochemical Dictionary*, Springer, Berlin, Heidelberg, **2008**.
[48] C. Moreno-Castilla, H. García-Rosero, F. Carrasco-Marín, *Materials* **2017**, *10*, 747.
[49] N. K. N. Quach, W. D. Yang, Z. J. Chung, H. L. Tran, *Adv. Mater. Sci. Eng.* **2017**, *2017*, 1–9.
[50] A. Elmouwahidi, E. Bailón-García, A. F. Pérez-Cadenas, F. Carrasco-Marín, *Wood Sci. Technol.* **2020**, *54*, 401–420.
[51] G. Tobias, L. Shao, C. G. Salzmann, Y. Huh, M. L. H. Green, *J. Phys. Chem. B* **2006**, *110*, 22318–22322.
[52] M. P. Chavhan, S. Ganguly, in *Mater Today Proc*, Elsevier Ltd, **2018**, pp. 9754–9759.
[53] J. Wang, S. Kaskel, *J. Mater. Chem.* **2012**, *22*, 23710–23725.
[54] C. Alegre, M. E. Gálvez, E. Baquedano, E. Pastor, R. Moliner, M. J. Lázaro, *Int. J. Hydrogen Energy* **2012**, *37*, 7180–7191.
[55] D. Hulicova-Jurcakova, M. Seredych, G. Q. Lu, T. J. Bandosz, *Adv. Funct. Mater.* **2009**, *19*, 438–447.
[56] T. Asset, P. Atanassov, *Joule* **2020**, *4*, 33–44.
[57] F. Jaouen, M. Lefèvre, J. P. Dodelet, M. Cai, *J. Phys. Chem. B* **2006**, *110*, 5553–5558.
[58] S. H. Lee, J. Kim, D. Y. Chung, J. M. Yoo, H. S. Lee, M. J. Kim, B. S. Mun, S. G. Kwon, Y. E. Sung, T. Hyeon, *J. Am. Chem. Soc.* **2019**, *141*, 2035–2045.
[59] Y.-C. Wang, W. Huang, L.-Y. Wan, J. Yang, R.-J. Xie, Y.-P. Zheng, Y.-Z. Tan, Y.-S. Wang, K. Zaghib, L.-R. Zheng, S.-H. Sun, Z.-Y. Zhou, S.-G. Sun, *Sci. Adv.* **2022**, *8*, eadd8873.
[60] T. N. Tran, M. Y. Song, K. P. Singh, D. S. Yang, J. S. Yu, *J. Mater. Chem. A* **2016**, *4*, 8645–8657.
[61] J. Sanetuntikul, C. Chuaicham, Y. W. Choi, S. Shanmugam, *J. Mater. Chem. A* **2015**, *3*, 15473–15481.
[62] R. Gokhale, S. Thapa, K. Artyushkova, R. Giri, P. Atanassov, *ACS Appl. Energ. Mater.* **2018**, *1*, 3802–3806.
[63] S. Ratso, M. Käärik, M. Kook, P. Paiste, J. Aruväli, S. Vlassov, V. Kisand, J. Leis, A. M. Kannan, K. Tammeveski, *Int. J. Hydrogen Energy* **2019**, *44*, 12636–12648.
[64] Y. Wang, S. Berthon-Fabry, *Electrocatalysis* **2021**, *12*, 78–90.
[65] K. Artyushkova, A. Serov, S. Rojas-Carbonell, P. Atanassov, *J. Phys. Chem.* **2015**, *119*, 25917–25928.
[66] M. Monthioux, *Carbon N Y* **2020**, *160*, 405–406.
[67] A. Bianco, H. M. Cheng, T. Enoki, Y. Gogotsi, R. H. Hurt, N. Koratkar, T. Kyotani, M. Monthioux, C. R. Park, J. M. D. Tascon, J. Zhang, *Carbon N Y* **2013**, *65*, 1–6.
[68] Y. Wang, M. J. Larsen, S. Rojas, M. T. Sougrati, F. Jaouen, P. Ferrer, D. Gianolio, S. Berthon-Fabry, *J. Power Sources* **2021**, *514*, 230561.
[69] R. Ma, Y. Zhou, C. Hu, M. Yang, F. Wang, K. Yan, Q. Liu, J. Wang, *Energy Storage Mater.* **2018**, *13*, 142–150.
[70] L. Álvarez-Manuel, C. Alegre, D. Sebastián, M. J. Lázaro, *Int. J. Hydrogen Energy* **2023**, DOI 10.1016/j.ijhydene.2023.06.184.
[71] L. Álvarez-Manuel, C. Alegre, D. Sebastián, A. Eizaguerri, P. F. Napal, M. J. Lázaro, *Catal. Today* **2023**, *418*, 114067.
[72] M. Mazzucato, G. Daniel, A. Mehmood, T. Kosmala, G. Granozzi, A. Kucernak, C. Durante, *Appl. Catal. B* **2021**, *291*, 120068.
[73] A. A. Gewirth, J. A. Varnell, A. M. Diascro, *Chem. Rev.* **2018**, *118*, 2313–2339.
[74] M. Primbs, Y. Sun, A. Roy, D. Malko, A. Mehmood, M. T. Sougrati, P. Y. Blanchard, G. Granozzi, T. Kosmala, G. Daniel, P. Atanassov, J. Sharman, C. Durante, A. Kucernak, D. Jones, F. Jaouen, P. Strasser, *Energy Environ. Sci.* **2020**, *13*, 2480–2500.
[75] W. Kiciński, S. Dyjak, W. Tokarz, *J. Power Sources* **2021**, *513*, 230537.
[76] L. Osmieri, Q. Meyer, *Curr. Opin. Electrochem.* **2022**, *31*, 100847.
[77] A. H. A. Monteverde Videla, D. Sebastián, N. S. Vasile, L. Osmieri, A. S. Aricò, V. Baglio, S. Specchia, *Int. J. Hydrogen Energy* **2016**, *41*, 22605–22618.
[78] S. Komini Babu, D. Spernjak, R. Mukundan, D. S. Hussey, D. L. Jacobson, H. T. Chung, G. Wu, A. J. Steinbach, S. Litster, R. L. Borup, P. Zelenay, *J. Power Sources* **2020**, *472*, 228442.
[79] Y. Kim, L. P. Urbina, T. Asset, M. Secanell, P. Atanassov, J. Barralet, J. T. Gostick, *J. Power Sources* **2023**, *562*, 232741.
[80] A. Uddin, L. Dunsmore, H. Zhang, L. Hu, G. Wu, S. Litster, *ACS Appl. Mater. Interfaces* **2020**, *12*, 2216–2224.
[81] L. Jiao, J. Li, L. L. R. Richard, Q. Sun, T. Stracensky, E. Liu, M. T. Sougrati, Z. Zhao, F. Yang, S. Zhong, H. Xu, S. Mukerjee, Y. Huang, D. A. Cullen, J. H. Park, M. Ferrandon, D. J. Myers, F. Jaouen, Q. Jia, *Nat. Mater.* **2021**, *20*, 1385–1391.
[82] C. Lo Vecchio, A. Serov, M. Dicome, B. Zulevi, A. S. Aricò, V. Baglio, *Electrochim. Acta* **2021**, *394*, 139108.
[83] G. Zhang, R. Chenitz, M. Lefèvre, S. Sun, J. P. Dodelet, *Nano Energy* **2016**, *29*, 111–125.
[84] Y. Shao, J. P. Dodelet, G. Wu, P. Zelenay, *Adv. Mater.* **2019**, *31*, DOI 10.1002/ADMA.201807615.
[85] R. Chenitz, U. I. Kramm, M. Lefèvre, V. Glibin, G. Zhang, S. Sun, J. P. Dodelet, *Energy Environ. Sci.* **2018**, *11*, 365–382.

Manuscript received: October 11, 2023
Revised manuscript received: November 11, 2023
Version of record online: December 18, 2023